Magnetic properties of nested carbon nanostructures studied by electron spin resonance and magnetic susceptibility measurements

Shunji Bandow
Instrument Center, Institute for Molecular Science, Myodaiji, Okazaki 444, Japan

(Received 1 May 1995; accepted for publication 11 April 1996)

Nested carbon nanostructures, e.g., nanotubes and nanoballs, are separated from the coexisting materials of carbon flakes and needle-like fragments by sonication, centrifugalization and low-temperature combustion. Content of nanotubes at the final stage separation is in excess of 85% by weight. The nested carbon nanostructures (>85 wt % tubules) are studied by electron spin resonance (ESR) and magnetic susceptibility measurements. The temperature dependence of the conduction-ESR intensity for the nested carbons is similar to that for graphite. On the other hand, the g value is almost constant ($g=2.0096\pm0.0004$ at room temperature) between 40 and 300 K, in contrast to that of graphite. These ESR features are discussed in terms of the electronic structure of carbon nanotubes predicted by theoretical calculation. The magnetic field dependence of differential magnetic susceptibility (χ_{diff}) indicates a logarithmic divergence in the magnetic field $H\leqslant 2$ kG and the χ_{diff} is a positive value at $H\approx 0.8$ kG, which is qualitatively consistent with the magnetic properties of metallic carbon nanotube enunciated by Ajiki and Ando. © *1996 American Institute of Physics.* [S0021-8979(96)04514-8]

I. INTRODUCTION

The nested carbon nanostructures, e.g., nanotubes and nanoballs, were discovered as the by-products at the synthesis of fullerenes. The fullerenes themselves were obtained in soot generated by a dc arc discharge between the carbon rods mounted on the ends of positive and negative electrodes in a depressurized He gas.[1] On the other hand, the nested carbons were found in a carbonaceous deposit grown at the tip of the cathode carbon rod,[2] which was composed of bundles of fibrous carbons (inner part) and a hard shell (outer part). The nested carbons only existed at the inner part of the carbonaceous deposit with carbon allotropes such as micron graphite flakes and sp^2 carbon nanospheres.

The structure of nested carbons, especially for carbon nanotube, can be visualized by rolling up a graphene sheet to form seamless tubule (or by the shape of faceted multihedron for nanoball). Graphene itself is a zero-gap semiconductor.[3] However, when the flat sheet is rolled up and formed seamless tubule, it presents either semiconducting or metallic feature depending on the cyclic boundary condition around the tube wall or, simply, on the tube diameter.[4–7] The energy gap of the semiconducting tubule decreases with the decreasing tube diameter in order to match with that of a flat (infinite tube diameter) graphene sheet. The direct observation of the electrical transportation properties of the carbon nanotubes was carried out by Zhang and Lieber,[8] Seshadri *et al.*,[9] and Nakayama *et al.*[10] They detected the thermal activation type electric conduction due to the energy gaps ranging from 0.06 to 0.26 eV for various diameter tubules. However, Langer *et al.*[11] could not observe any semiconducting features for carbon nanotubes. The reason of the above contradiction is not clear, but may depend on the sample quality.

The interlayer spacing of concentric carbon nanotube was slightly greater (1%–2%)[12] than that of graphite, and the individual layers were considered to be coupled by the van der Waals interaction. Though the interlayer spacing was not large enough to separate the individual layers into an electronically isolated layer, a theoretical calculation for a concentric graphene double-wall tube showed that the electronic features of individual layers basically did not change even taking into account the interlayer interactions.[13] According to this theoretical calculation, the conductivity of concentric carbon nanotube normally reflects the electronic feature of the outer layer tubule due to smaller energy gap than that of the inner layer one. If Langer *et al.*[11] only measured the large diameter tubules, the semiconducting feature was hardly detected due to the small energy gaps for such large tubules.

Recently, a high yield synthesis condition for nested carbons was found,[14] and the electronic and vibrational features for carbon nanotubes were calculated by taking into account the cyclic boundary condition around the tube wall.[4–7,15–17] However, the experimental studies for purified carbon nanotubes have not yet been refined well in respect of the separation-purification,[18,19] the electronic,[8–11,20] and vibrational[17,21–23] features due to sample quality and quantity. As described previously, the micron graphite flakes and sp^2 carbon nanospheres coexist with the nested carbons. To separate the nested carbons from those impurity carbon allotropes, a newly developed method combined with sonication, centrifugalization, and combustion is introduced in this study. The magnetic properties of the separation-purified nested carbons are studied by electron spin resonance (ESR) and static magnetic susceptibility measurements.

II. EXPERIMENT

The nested carbons were synthesized by a conventional dc carbon arc discharge method.[2,14] 5 mm in diameter carbon rods were burnt by an arc current of 50 A under a static He pressure of 400 Torr with a constant spark gap of ~1 mm. The inner part (crude inner deposits or bundles of fibrous carbons) of the carbonaceous deposit grown at the tip of the cathode carbon rod was carefully scraped from the outer part

 0021-8979/96/80(2)/1020/8/$10.00

of the carbonaceous deposit. These crude inner deposits separated into the nested carbons and graphite flakes by using sonication, centrifugalization, and combustion.

The weight loss due to combustion for carbon materials was recorded by a Dupont 951 thermogravimetric analyzer. The sample for combustion was placed in a platinum pan hanged on electrobalance and heated up to 350 °C in a flow of dry air. For the electron microscope observation, various samples were ultrasonically dispersed in ethanol, and one drop of this solution was placed onto the sample plate for high-resolution scanning electron microscopy (HRSEM) or onto the carbon microgrid for transmission electron microscopy (TEM). A HITACHI S-900 (HRSEM) and a Philips EM400 (TEM), whose acceleration voltages were selected at 5 and 120 kV, respectively, were used for taking micrographs. The powder x-ray diffraction was measured by a MAC Science MXP3VA at room temperature. A copper x-ray tube was used as an x-ray source and the diffraction signal was monochromatized by a graphite crystal placed in front of the x-ray counter. The ESR spectra were recorded by both a Varian E112 and a Bruker ESP300E spectrometers operated at *X* band (9.480 GHz) with a magnetic field modulation frequency of 100 kHz. The microwave frequency and magnetic field were measured by a Hewlett Packard 5352B microwave frequency counter and a Bruker ER035M NMR gaussmeter, respectively. An Oxford ESR-900 liquid He flow cryostat was used for temperature variation, and DPPH (1,1-diphenyl-2-picrylhydrazyl) was used to determine the spin concentration. The static magnetic susceptibility was measured by a high sensitivity Faraday balance (main design from an Oxford Instrument) in the temperature range from 2 to 260 K, and the magnetization was recorded against the magnetic field up to 55 kG. The sample was placed in a quartz cell and fixed by a paraffin liquid. The contribution of blank materials (quartz cell and paraffin liquid) to the magnetic susceptibility was carefully corrected.

III. RESULTS AND DISCUSSION

A. Sample separation and structural characterization

The HRSEM images of crude inner deposits (bundles of fibrous carbons) are shown in Fig. 1(a) (low magnification) and 1(b) (high magnification). In Fig. 1(a), two fibrous carbons are partially seen. The size of these carbons mostly ranged from 50 to 60 μm in diameter and from 3 to 5 mm in length. The high magnification image [Fig. 1(b)] indicated the existence of very small fibers attaching on the surface. To suspend these small fibers into a solution (50% of methanol diluted by distilled water), an ultrasonic agitation was used. After 1 h sonication, the fibrous carbons separated into two parts: one was the needle-like fragments (NP) by ~70 wt % as a precipitate and the other was the suspended particles (S-1) by ~30 wt % in a liquid above the precipitate. The HRSEM images of NP are shown in Fig. 1(c) (low magnification) and 1(d) (high magnification); the shape and length were almost the same as that of fibrous carbons [Fig. 1(a)] but the diameter reduced 10%–15% as shown in Fig. 1(c). The high magnification image [Fig. 1(d)] indicated flaky structure instead of small fibers.

The powder x-ray diffraction pattern for NP [Fig. 2(a)] indicated usual graphitic structure but lack of clear *hkl* reflections, which suggests the existence of stacking mismatch between the interlayer planes (turbostratic nature). Combining the results of HRSEM [Fig. 1(d)] and x-ray diffraction, we can conclude that the sample NP is turbostratic graphite. The lattice parameters of NP were found to be $a=0.2455 \pm 0.0004$ nm (from 10, 11, and 20 reflections) and $c=0.6847 \pm 0.0006$ nm (from 002 and 004 reflections). It is worth to note that the sample NP is an assembly of turbostratic graphite, and the small fibers (or crude carbon nanotubes) stay in the suspension liquid.

After driving off the solution of the suspension by a rotary evaporator at 60 °C, the small fibers (S-1) remained were dispersed into distilled water with 0.1% of cationic surfactant (benzalkonium chloride, Kanto Chemical Co.), which allowed them to stay suspending as a colloid. Anionic surfactant (Aerosol OT) was also used to check up the dispersability for S-1, but it gave much poorer result. The colloidal suspension of S-1 was then placed in a centrifuge cell and spun at 5000 rpm for 30 min to remove graphite or carbon flakes as a precipitate. The suspension liquid above the precipitate was decanted and the solution was evaporated by the same way stated above. The solids (S-2) remained were washed by methanol to remove excess surfactant and dried by a rotary evaporator. Finally, S-2 was heated at 350 °C for 5 h in dry air (S-3). About 10% loss in weight was observed at this final process. This weight loss may be due to gasification of carbon impurities, since the burning of tubules started at the tip part[18,24] and the TEM image (Fig. 3) showed the tips of carbon nanotubes even after the above heat treatment; there is no fact of initiating the burning of tubules. A summary of separation process is shown in Fig. 4 with the sample identification (ID) codes of NP, S-1, S-2, and S-3, which refer to as ''needle precipitation'' (for needle-like fragments), ''stage-1,'' ''stage-2,'' and ''stage-3,'' respectively.

According to the HRSEM and TEM studies, the final stage sample S-3 was a mixture of multiwall carbon nanotubes and nested carbon nanoballs. Therefore, S-3 can be called the nested carbon nanostructures. The sizes of multiwall carbon nanotubes frequently ranged from 10 to 15 nm in outer diameter with several microns in length and 10 to 20 for the number of graphitic carbon layers, and of nested nanoballs frequently ranged from 15 to 30 nm in outer diameter and 20 to 30 for the number of graphitic carbon layers.

To estimate the content of multiwall carbon nanotubes by weight in S-3, the following procedure was carried out: First, the number of tubules and of balls in an area (0.5×0.5 μm^2) of TEM image were counted. According to the counting at several different areas, 30%–40% tubules were obtained for S-3. Next, to calculate the volumes of tubule and ball, the dimensions of them were selected to be the median size (from TEM): 13 nm in diameter, 0.5 μm in length (restricted by a width of sampling area), and 3 nm in diameter of cylindrical hollow for tubule, and 23 nm in diameter and 6 nm in diameter of spherical hollow for ball. Assuming the same density for tubule and ball, we finally obtained the tubule content in excess of 85% by weight. Therefore, we

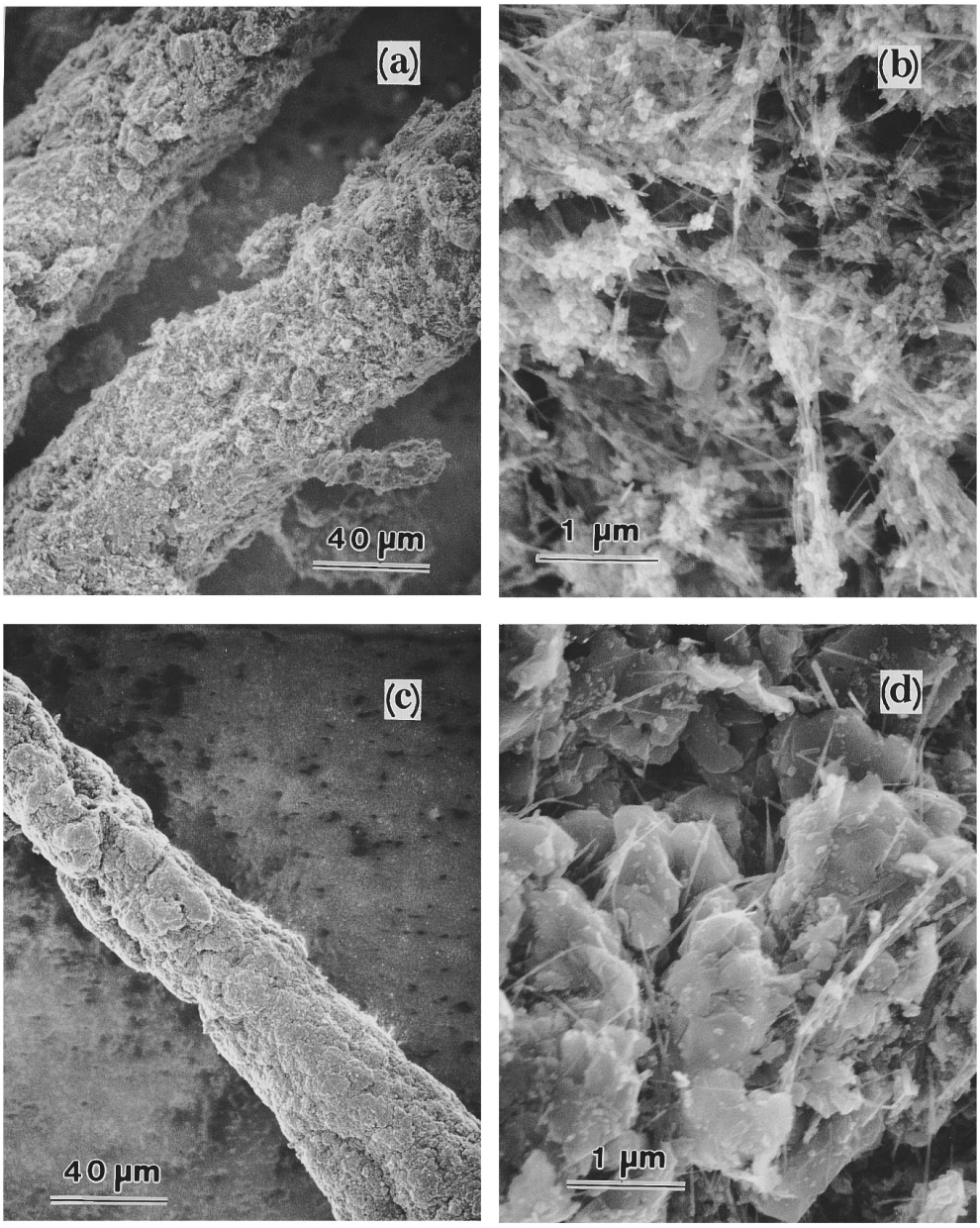

FIG. 1. Scanning electron microscopy images for cathode deposits. (a) and (b) were taken from the bundle of fibrous carbons (crude inner deposits) obtained from an inner part of cathode deposit. (c) and (d) were from the sonication-separated needle-like fragments (NP). The low magnification images (a) and (c) show a part of the fibrous carbons and of NP, respectively. The high magnification images (b) and (d) present different surface information: small fibers can be seen for the crude inner deposits, but micron flakes for NP.

can say that most of the contents in S-3 are the multiwall carbon nanotubes. To increase the content of tubules, further combustion at high temperature (500 °C for 60 min, and 70 wt % loss) was also carried out. However, the tubule content did not show any significant difference before and after above treatment.

The powder x-ray diffraction pattern of S-3 also showed the turbostratic nature [Fig. 2(b)]. The lattice parameters for S-3 were found to be $a=0.2450\pm0.0004$ nm (from 10, 11, and 20 reflections) and $c=0.6802\pm0.0006$ nm (from 002 and 004 reflections), which are almost the same with those for NP. The diffraction patterns for NP and S-3 were essentially identical in shape, but the linewidth of 002 for S-3 was about twice broader than that for NP, which is due to the smaller number of graphene sheets for S-3 than that for NP. According to the x-ray diffraction, the intra- and interlayer local structure for NP and S-3 were similar to each other. However, they have different form of graphene sheets: for NP, the form is basically the same as that of micron graphite flakes; on the other hand, for S-3, the form can be visualized by rolling up the layered graphene sheets to form concentric cylinder or sphere.

B. ESR for nested carbon nanostructures

The ESR spectra for S-1, S-2, and S-3 are shown in Fig. 5. Two spectral components (narrow and broad ESR lines) can be clearly seen for S-2 and S-3. For the narrow compo-

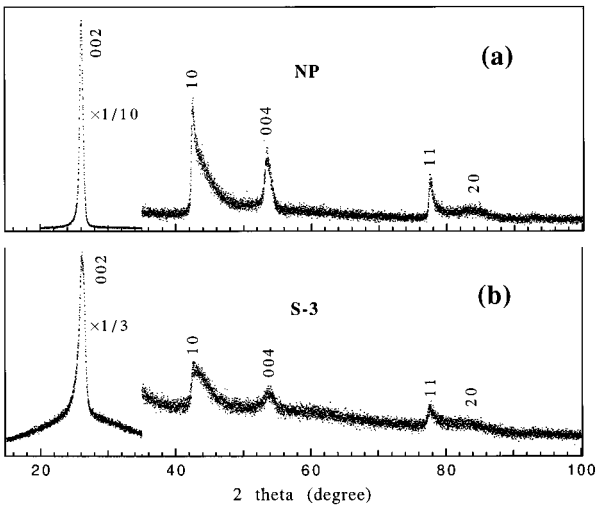

FIG. 2. Charts of powder x-ray diffraction. (a) the sonication-separated needle-like fragments (NP) and (b) the nested carbon nanostructures (S-3). The reflection indexes are indicated around peak maxima. The source of x ray is Cu $K\alpha$.

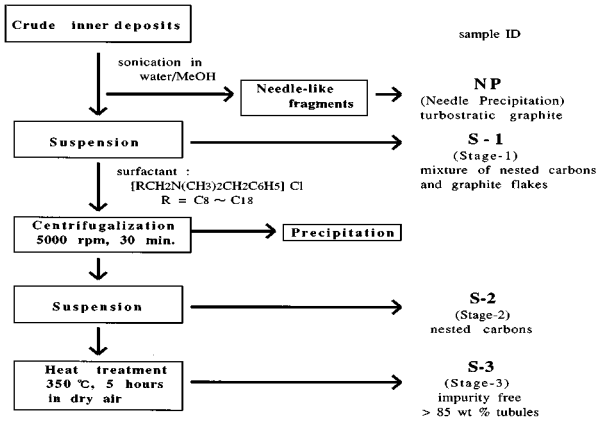

FIG. 4. Flow chart of separation precess. Sample ID is the identification code for various stages of sample: NP, S-1, S-2, and S-3 refer to ''needle precipitation'' (for sonication-separated needle-like fragments), ''stage-1,'' ''stage-2,'' and ''stage-3,'' respectively. NP was turbostratic graphite, S-1 a mixture of the nested carbon nanostructures (tubules and balls) and graphite flakes, S-2 the nested carbon nanostructures, and S-3 the impurity-free nested carbon nanostructures including tubules concentrated over 85% by weight.

nent ($g=2.0026\pm0.0002$), the ESR intensity decreased by an order of magnitude after the heat treatment. Furthermore, regardless of the heat treatment, the temperature dependence of this narrow component behaved as Curie-like, reminiscent of a impurity signal. Therefore, we conclude that the narrow component associates with an extrinsic origin, and will not pursue this component.

A g value of S-1 (2.0137 ± 0.0002) was comparable to that of polycrystalline graphite (2.0182) estimated by $(g_{\parallel}+2g_{\perp})/3$, where $g_{\parallel}$ (2.0495) and $g_{\perp}$ (2.0026) are the g values at room temperature with the magnetic fields applied parallel and perpendicular to the c axis, respectively.[25] The electronic structure of a two-dimensional (2D) graphite (neglecting an interlayer interaction between graphene sheets) is characterized by zero energy gap and zero density of state at the Fermi level (zero-gap semiconductor).[3] Furthermore, the large $g_{\parallel}$ for graphite originates in such electronic features, because the g shift from the free-electron value ($\Delta g_e=g-g_e$) is proportional to $\lambda/\Delta E$ for semiconductors,[26] where g_e is the g value of free electron (2.0023), λ the spin-orbit coupling constant, and ΔE the energy separation to the nearest band being mixed by spin-orbit coupling. For example, $\lambda=3.7$ meV and $\Delta E=17$ meV were used to evaluate $g_{\parallel}$ for a three-dimensional (3D) graphite (real graphite with weak interlayer interaction), resulting in $\Delta g_e\approx0.2$.[25] The large g value for S-1 (2.0137) probably indicates the existence of polycrystalline or flakes of graphite at this separation stage. For S-2, however, the g value of broad component reduced to 2.0095 ± 0.0002 and this value did not change within the experimental error even after the heat treatment ($g=2.0096\pm0.0004$ for S-3). The change of g value from

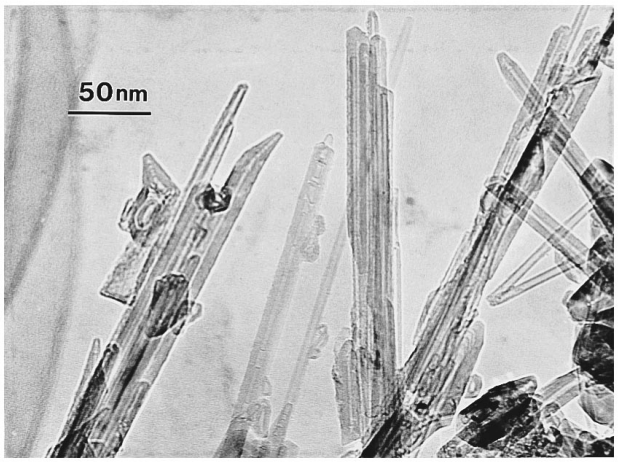

FIG. 3. Transmission electron microscopy image for nested carbon nanostructures. The sample was heated at 350 °C for 5 h in dry air. Tips of tubules are clearly seen.

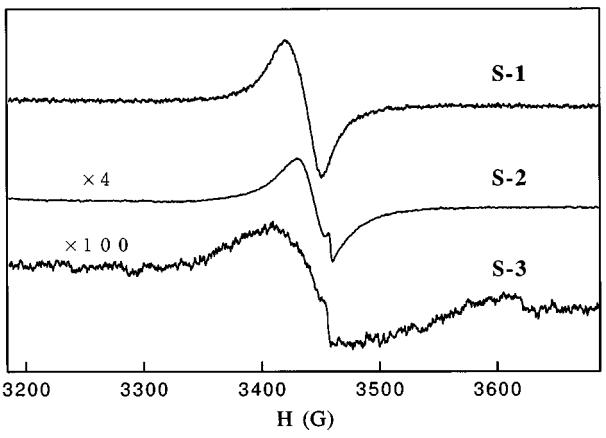

FIG. 5. ESR spectra for various separation stages. The spectra were taken at room temperature with a microwave frequency of 9.480 GHz. Two spectral components (narrow and broad ESR lines) can be seen for S-2 and S-3, and one broad component for S-1. The g values for the broad component of S-1, S-2, and S-3 were 2.0137 ± 0.0002, 2.0095 ± 0.0002, and 2.0096 ± 0.0004, respectively, and that for the narrow one was 2.0026 ± 0.0002. The integrated ESR intensities of broad component for S-2 and S-3 were in the same order of magnitude, 10^{-8} emu/g.

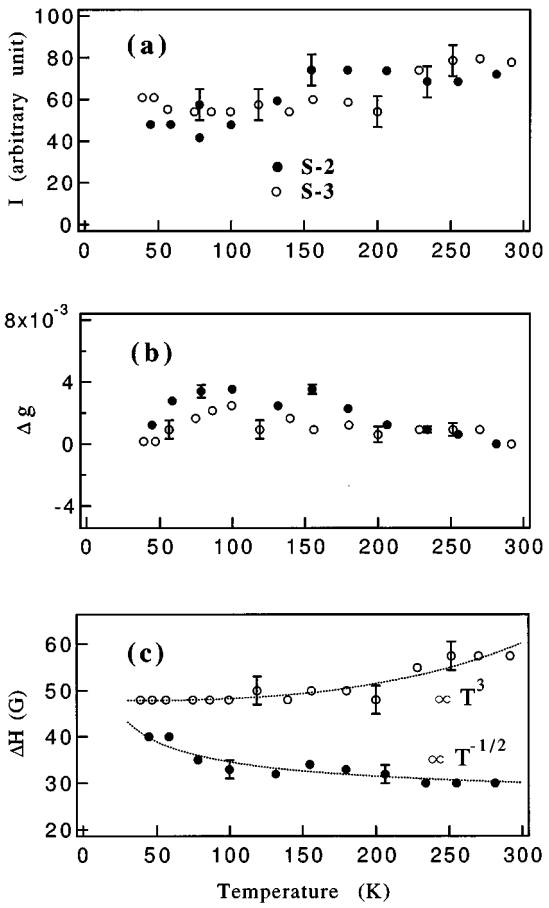

FIG. 6. Temperature dependences of (a) integrated ESR intensity (I) of broad component, (b) g shift (Δg) from room-temperature value and (c) linewidth (ΔH) of broad component for nested carbon nanostructures. Closed and open circles are for S-2 and S-3, respectively. Dotted lines in (c) represent T^3 and $T^{-1/2}$ dependences. Vertical bars indicate the experimental error.

2.0137 (for S-1) to 2.0095 (for S-2) should be due to a removal of the polycrystalline or flakes of graphite from the sample by centrifugal separation.

The temperature dependences of integrated ESR intensity (I), g shift (Δg) from room-temperature value and linewidth (ΔH) for S-2 or S-3 are shown in Figs. 6(a), 6(b), and 6(c), respectively. The I decreased 20%–30% upon decreasing the temperature from ~280 to 40 K for both S-2 and S-3 [Fig. 6(a)], which is compatible with the temperature behavior of the Pauli paramagnetism of graphite evaluated from the band parameters by McClure.[25,27] The magnitude of spin magnetic susceptibility associated with the broad component was estimated to be of the order of 10^{-8} emu/g, indicating the same order as that of graphite.[25] Therefore, we conclude that the broad ESR signal stems from conduction electrons.

The Δg ($\leqslant 0.002$) for S-2 or S-3 showed weaker temperature dependence [Fig. 6(b)], by an order of magnitude, than that for graphite. In graphite, the main term of the temperature dependence of Δg is from $g_{\|}$ (g value for the intralayer conduction in graphene sheet), which varies 0.0775 between room temperature and 77 K.[25] Although the origin of the temperature dependence of Δg for graphite has not been analyzed theoretically, it probably depends on the zero-gap semiconducting feature (degenerate band-edge structure) for 2D graphite; the thermal excitation of electrons to the upper energy level can easily occur and modify the ground state of electrons. This modification of ground-state properties may cause the large temperature dependence of Δg, since the g value is sensitive to the circumstances of the electrons. For such a reason, the weaker temperature dependence of Δg for S-2 or S-3 probably originates from the different band-edge structure for carbon nanotube: according to the theoretical calculation,[4–7] the carbon nanotube can be either semiconductor or metal depending on the cyclic boundary conditions around tube wall, allowing a finite ΔE for semiconducting tubule or a finite density of state at the Fermi level for metallic tubule unlike 2D graphite. The difference in electronic structure between carbon nanotube and graphite would suppress the thermal excitation effect for carbon nanotubes, resulting in the present temperature dependences of Δg for S-2 and S-3.

According to the relation $\Delta g_e \propto \lambda/\Delta E$ for semiconductors,[26] small Δg_e can be expected for semiconducting tubules due to finite ΔE. Moreover, Δg_e for metals was qualitatively explained by Yafet[28] using a relation $\Delta g_e \propto \lambda$, which results in a small Δg_e for metallic tubules due to small λ for the carbon. Therefore, small Δg_e can be expected for both semiconducting and metallic tubules. The present experiments indicated relatively small Δg_e for both S-2 ($0.0072 = 2.0095 - g_e$) and S-3 ($0.0073 = 2.0096 - g_e$), unlike large Δg_e for graphite ($0.0159 = 2.0182 - g_e$). This result does not contradict with above expectation for Δg_e.

Kosaka *et al.*[29] observed almost temperature independent Δg for carbon nanotubes after annealing at 2850 °C *in vacuo* as well as for our S-3 (or S-2). However, their g value was different from our observation; they observed the ESR signals at $g = 2.012$ and 2.0022 for carbon nanotubes before and after the annealing, respectively. Our g value (2.0096) for S-3 (or 2.0095 for S-2) was comparably close to their g value (2.012) for carbon nanotubes before the annealing, while their g value (2.012) indicated large temperature dependence in contrast to the temperature behavior of Δg for S-3 (or S-2). In terms of the g value, the ESR features seem to have a contradiction between S-3 (or S-2) and their samples. However, after analyzing the temperature behavior of ΔH, the ESR features for our samples can be explained as indicates below.

In the observation by Kosaka *et al.*,[29] ΔH at 4 K was broader than that at 296 K regardless of the annealing condition of the sample, i.e., ΔH increased with decreasing temperature. In our case, ΔH increased with decreasing temperature for S-2, however, ΔH decreased with decreasing temperature for S-3. The curve-fitting results for ΔH indicated $T^{-1/2}$ and T^3 dependences for S-2 and S-3, respectively, as shown in Fig. 6(c) by the dotted lines, where T is the temperature. It is known that the relation $\Delta H \propto T^{-1/2}$ is typical for the conduction electrons being scattered by an interaction through the spin-orbit coupling of impurity atoms.[25,30] Therefore, for S-2, it is reasonable to consider that the scattering of conduction electrons mainly takes place at the impurity sites existing in the sample. For S-3, as stated above, the temperature dependence of ΔH is represented by

T^3. The T^3 dependence of ΔH was calculated by Elliott[26] for semiconductors and metals under the assumptions that the conduction electrons were scattered by the lattice vibrations and the temperature was lower than the Debye temperature. As described previously, the Curie-like component decreased by an order of magnitude before and after the heat treatment (see S-2 and S-3 in Fig. 5), which suggests that the impurities or defects existing initially in the nested carbons have been removed by the heat treatment. Therefore, the scattering of conduction electrons came to be dominated by the lattice vibrations instead of the impurities, resulting in $\Delta H \propto T^3$ for S-3. In other words, the sample S-3 is almost impurity or defect free.

C. Magnetic susceptibility for nested carbon nanostructures

Magnetic susceptibility, $\chi = M/H$ (M stands for the magnetization and H for the magnetic field), was measured for NP and S-3. NP was ground by agate mortar to avoid orientational effect due to the needle shape. On the other hand, S-3 was used without further grind because of the randomness in orientation of tubules. The temperature dependences of χ were measured at two magnetic fields, 21 kG (for NP and S-3) and 2 kG (for S-3), and are shown in Fig. 7(a) (normal coordinates) and 7(b) (logarithmic coordinates). Previously, we concluded that the sample NP was the assembly of micron flakes of turbostratic graphite, but not of tubules. However, the magnitude and temperature dependence of χ for NP were almost the same as the data for carbon nanotubes reported by Heremans *et al.*[31] and Ramirez *et al.*[32] The reason of this contradiction is possibly due to the sample quality; their samples included a number of needle-like fragments NP).

According to the studies by Ganguli and Krishnan[33] and also by Poquet *et al.*,[34] the χ for HOPG (highly oriented pyrolytic graphite) indicated large anisotropy between $\chi_{\|}$ and $\chi_{\perp}$, where $\chi_{\|}$ and $\chi_{\perp}$ are the χ with the magnetic field applied parallel and perpendicular to the c axis, respectively. The decrease of $\chi_{\|}$ was observed for $T \geqslant 100$ K as shown in Fig. 7(b). Such temperature dependence and anisotropy of χ for HOPG were analyzed theoretically by Sharma *et al.*[35] by using the energy band parameters of perfectly pure graphite. They also calculated several temperature dependences of χ by changing the band parameters. For NP, the temperature behavior of χ was essentially identical with that ($\chi_{\|}$) for HOPG, which can be confirmed by arbitrarily shifting the temperature axis in Fig. 7(b). According to the calculation by Sharma *et al.*,[35] the temperature behavior of χ was sensitively affected by the band parameters, which are sensitive to a change in lattice parameters and a defect content. Since NP was the assembly of micron flakes of turbostratic graphite, the temperature dependence of χ for NP may be obtained by changing the energy band parameters of HOPG.

Here we discuss the leading term of χ. In the present case, χ can be divided into three terms: (1) the Pauli paramagnetic contribution due to the conduction electrons (10^{-8} emu/g from ESR), (2) the diamagnetism of the C^{4+} ion (-1.2×10^{-8} emu/g),[36] and (3) the orbital diamagnetism of conduction electrons due to a change in the band energy.

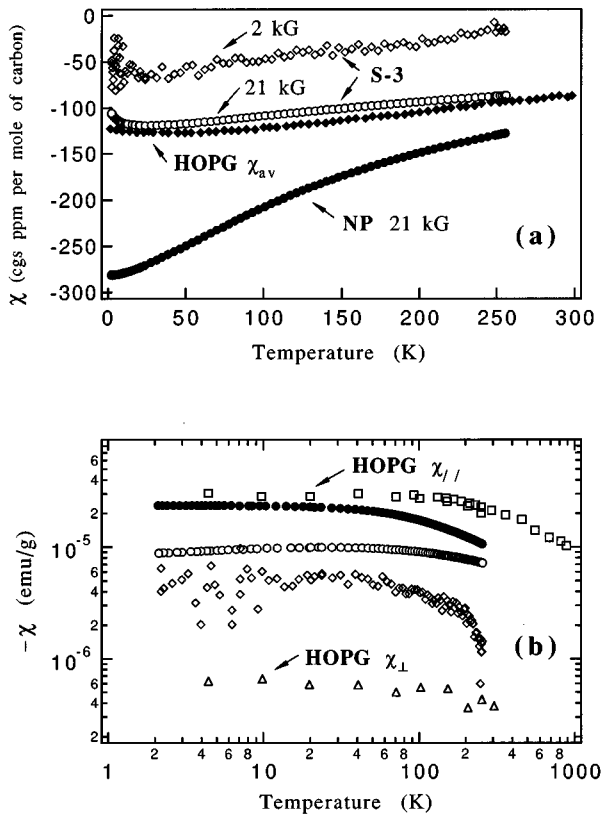

FIG. 7. Temperature dependence of magnetic susceptibility (χ). (a) is represented by molar unit, and (b) by gram unit with logarithmic scale. Open circles and open diamonds are for S-3 taken at the magnetic fields of 21 and 2 kG, respectively. Closed circles are for S-2 at 21 kG. The χ_{av} (closed diamonds) is the χ for orientationally averaged HOPG (highly oriented pyrolytic graphite) measured by Ramirez *et al.*. The $\chi_{\|}$ (open squares) and $\chi_{\perp}$ (open triangles) are the χ for HOPG with the magnetic field applied parallel and perpendicular to the c axis, respectively, measured by Heremans *et al.* and by Ganguli and Krishnan.

Since the observed values were of the order of 10^{-6} emu/g [Fig. 7(b)], the first or second term contribution is very small (order of 10^{-8} emu/g). In another word, the χ obtained in the present experiments are mainly associated with the third term (orbital diamagnetism).

For S-3, small magnitude of diamagnetic susceptibilities and weak temperature dependence of χ can be seen in Fig. 7(a). Furthermore, the magnitude of χ depends on H, which stems from an anomaly of M [see Fig. 8(a) for S-3] observed for $H \leqslant 2$ kG, because χ was simply defined by M/H. Such anomaly of M sometimes originates from ferromagnetic impurities. However, we can exclude such an extrinsic effect by the following reasons: (1) the sample NP did not show any anomaly of M at low H as shown in Fig. 8. (2) If the anomaly stems from the ferromagnetic impurities such as Fe, Co, and Ni, the impurity content is estimated to be 70–80 ppm. However, the ferromagnetic impurities (Fe and Ni) included in the original carbon rod are less than 1 ppm, which is far below the estimated value. (3) No ESR signal due to ferromagnetic materials was observed, which usually give very board ESR spectrum (ΔH of several hundreds gauss). Therefore, we conclude that the anomaly of M observed for $H \leqslant 2$ kG is an intrinsic feature for S-3.

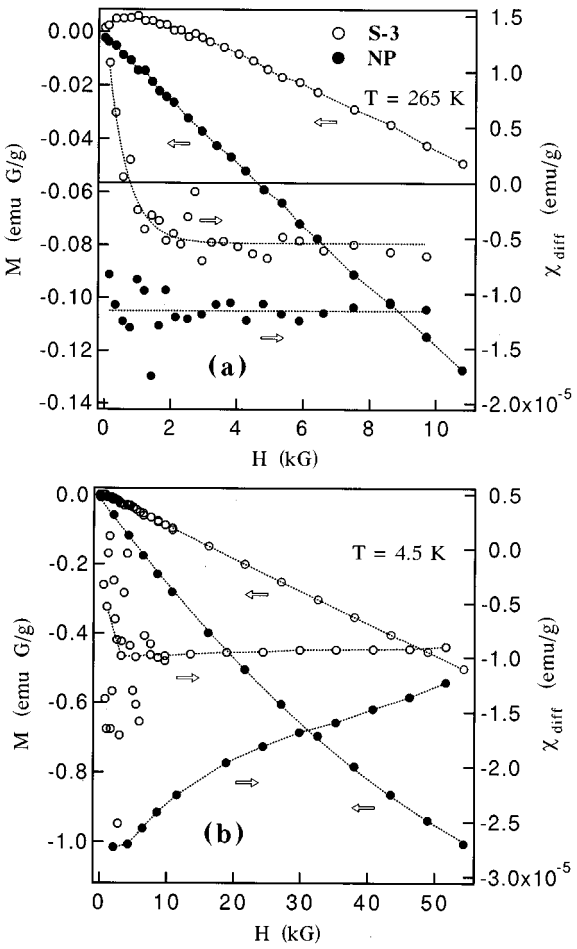

FIG. 8. Magnetic field dependences of magnetization (M) and differential magnetic susceptibility (χ_{diff}). (a) was taken at 265 K with the magnetic field (H) up to 11 kG, and (b) at 4.5 K up to 55 kG. Closed and open circles are for S-2 and S-3, respectively. The $\chi_{\text{diff}}(=dM/dH)$ were calculated by averaging over three points for $H<11$ kG and over two points for $H>11$ kG. Dotted lines are for the eye guide.

Since the M was not linearly proportional to H at low magnetic fields, the differential magnetic susceptibilities ($\chi_{\text{diff}}=dM/dH$) were calculated for NP and S-3, and are shown in Figs. 8(a) and 8(b) (data taken at 4.5 K are rather scattered than those at 265 K due to the unavoidable convection current of He heat exchange gas filled in the sample space). For $T=265$ K, the χ_{diff} for NP did not indicate any anomaly within the experimental error at low magnetic fields; in contrast to NP, an abrupt increase of χ_{diff} for $H\leqslant 2$ kG was observed for S-3, and the χ_{diff} reached to a positive value at $H\approx 0.8$ kG for $T=265$ K. According to the calculation by Ajiki and Ando,[37] the $\chi_{\text{diff}\parallel}$ (χ_{diff} with H applied parallel to the tubule axis) for metallic tubule diverges logarithmically at low magnetic fields and becomes positive infinite, while the $\chi_{\text{diff}\parallel}$ for semiconducting one does not diverge at low magnetic fields. The $\chi_{\text{diff}\perp}$ (χ_{diff} with H applied perpendicular to the tubule axis) for both semiconducting and metallic tubules do not indicate any singular point but indicate diamagnetic susceptibilities larger by an order of magnitude than $\chi_{\text{diff}\parallel}$. In order to compare the χ_{diff} for S-3 and the theoretical predictions,[37] the magnetic field dependence of χ_{diff} taken at 265 K was plotted against $\log(H)$ as shown in Fig. 9. For the magnetic field lower than ~2 kG, a logarithmic increase of χ_{diff} with decreasing H can be seen in this figure, as predicted by the theoretical calculation for metallic tubules. Therefore, we conclude that the anomaly of M observed for S-3 stems from the metallic character of carbon nanotubes included in the sample by a majority (>85 wt %).

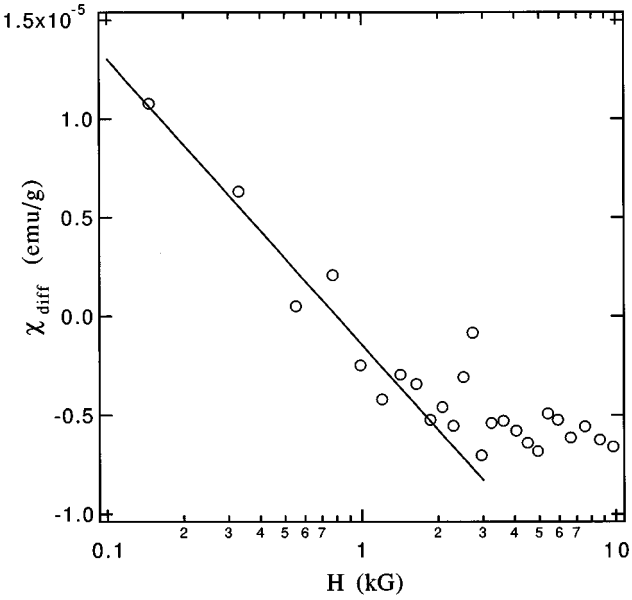

FIG. 9. Magnetic field dependence of differential magnetic susceptibility (χ_{diff}) represented by semilogarithmic scale. Data are for S-3 at 265 K. The χ_{diff} was linearly proportional to $\log(H)$ in the magnetic field (H) lower than ~2 kG and came to be a positive value at $H\approx 0.8$ kG.

So far, no theoretical calculation related to the electronic feature has been carried out for nested carbon nanoball. Provided that some nanoballs have metallic feature, the itinerant electrons move along quantized cyclotron orbits in H, and this cyclotron motion is restricted by a finite cage size of nanoball, i.e., the largest diameter of cyclotron motion is the same as the diameter of nanoball. The radius of the quantized cyclotron motion with the lowest energy is represented by $\sqrt{\hbar c/eH}$, where $\hbar$ is the Planck's constant divided by 2π, c the velocity of light, and e the electron charge. Therefore, for the metallic nanoball with a diameter of several tens nm, the corresponding H is estimated to be of the order of 10 kG. When H is lower than this value, the energy spectrum for the finite system cannot be quantized any longer unlike bulk one, which also results in an anomaly of the orbital magnetism at low magnetic fields. This anomaly of M was observed in the ultrafine Mg particles with an average diameter of 20 nm by Ida and Kimura.[38] We think that the M anomaly probably exists for metallic carbon nanoballs, not only for metallic carbon nanotubes. However, since the nanoball content in S-3 was less than 15 wt %, a contribution to M of metallic nanoballs is much smaller than that of metallic tubules (>85 wt % tubules).

It was calculated that one third of single-wall tubules (graphene tubule) could be metal (others were semiconductor) by varying tube diameter.[4–7] For double-wall tubules, the electronic features of individual layers of concentric tubule remained even after the interlayer interaction was

considered.[13] According to these theoretical calculations, we can imagine a concentric multiwall tubule with an inner metallic tubule covered by an outer semiconducting one, and vice versa. Since the existence of metallic tubules was confirmed for S-3, some parts (maybe one third) of constituent layers of multiwall tubule should exhibit a metallic feature and other constituent layers should do a semiconducting one. This means that the nanometer scale (but micron in length) metal-insulator (or -semiconductor) interface is realized in a piece of multiwall tubule.

IV. CONCLUSIONS

The inner part of the arc derived crude cathode deposit was separated into (1) needle-like fragments, (2) carbon flakes, and (3) nested carbon nanostructures by sonication and centrifugal separation using a cationic surfactant (benzalkonium chloride). The first and second materials were turbostratic graphite, while the third ones were a mixture of multiwall carbon nanotubes and nested carbon nanoballs. The concentration of multiwall carbon nanotubes in the third sample was in excess of 85% by weight. The magnetic properties of the nested carbon nanostructures (or simply say multiwall carbon nanotubes because of the tubule content) were studied by ESR and χ measurements. The ESR study indicated the existence of conduction electrons with almost temperature-independent smaller g value (2.0096) than that of polycrystalline graphite (2.0182). This smaller g value suggested that the band-edge structure for the nested carbons was different from that of graphite. It was also found that the low-temperature combustion at 350 °C for 5 h in dry air was effective to remove impurities or defects from the sample. The χ_{diff} for the nested carbons indicated a logarithmic increase with decreasing H for $H \leqslant 2$ kG and reached to a positive value at $H \approx 0.8$ kG, which is qualitatively consistent with the theoretical prediction done by Ajiki and Ando[37] for metallic carbon nanotube. According to the theoretical prediction by Saito *et al.*,[13] the interlayer interaction between individual layers was too weak to change the electronic structure of each individual layer of multiwall carbon nanotube. In addition, our experiments suggested an existence of metallic tubules. Therefore, we concluded that some parts (one third) of constituent layers of concentric tubule were metallic and other constituent layers (two third) were semiconducting. In other words, the nanometer scale (but micron in length) metal-insulator (or-semiconductor) interface should exist in a piece of multiwall carbon nanotube.

ACKNOWLEDGMENTS

The author expresses his appreciation to Professor K. Kimura for sending the papers related to the anomaly of orbital magnetism in finite system, and to Dr. P. Wang for her critical reading of the manuscript. Thanks are due to Electron Microscope center, National Institute for Physiological Science for the use of a Philips EM400 transmission electron microscope.

[1] W. Krätschmer, L. D. Lamb, K. Fostiropoulos, and D. R. Huffman, Nature **347**, 354 (1990).
[2] S. Iijima, Nature **354**, 56 (1991).
[3] P. R. Wallace, Phys. Rev. **71**, 622 (1947).
[4] N. Hamada, S. Sawada, and A. Oshiyama, Phys. Rev. Lett. **68**, 1579 (1992).
[5] K. Hiragaya, Phys. Rev. B **45**, 12071 (1992).
[6] R. Saito, M. Fujita, G. Dresselhaus, and M. S. Dresselhaus, Appl. Phys. Lett. **60**, 2204 (1992); Phys. Rev. B **46**, 1804 (1992).
[7] K. Hiragaya and M. Fujita, Phys. Rev. B **47**, 16563 (1992).
[8] Z. Zhang and C. M. Lieber, Appl. Phys. Lett. **62**, 2792 (1993).
[9] R. Seshadri, H. N. Aiyer, A. Govindaraj, and C. N. R. Rao, Solid State Commun. **91**, 195 (1994).
[10] Y. Nakayama, S. Akita, and Y. Shimada, Jpn. J. Appl. Phys. **34**, L10 (1995).
[11] L. Langer, L. Stockman, J. P. Heremans, V. Bayot, C. H. Olk, C. Van Haesendonck, Y. Bruynseraeda, and J-P. Issi, J. Mater. Res. **9**, 927 (1994).
[12] Y. Saito, T. Yoshikawa, S. Bandow, M. Tomita, and T. Hayashi, Phys. Rev. B **48**, 1907 (1993).
[13] R. Saito, G. Dresselhaus, and M. S. Dresselhaus, J. Appl. Phys. **73**, 494 (1993).
[14] T. W. Ebbesen and P. M. Ajayan, Nature **358**, 220 (1992).
[15] R. A. Jishi, L. Venkataraman, M. S. Dresselhaus, and G. Dresselhaus, Chem. Phys. Lett. **209**, 77 (1993).
[16] R. A. Jishi, L. Venkataman, M. S. Dresselhaus, and G. Dresselhaus, Phys. Rev. B **51**, 11176 (1995).
[17] P. C. Eklund, J. M. Holden, and R. A. Jishi, Carbon **33**, 959 (1995).
[18] T. W. Ebbesen, P. M. Ajayan, H. Hiura, and K. Tanigaki, Nature **367**, 519 (1994).
[19] H. Hiura, T. W. Ebbesen, and K. Tanigaki, Adv. Mater. **7**, 275 (1995).
[20] K. Tananka, T. Sato, T. Yamabe, K. Okahara, K. Uchida, M. Yumura, H. Niino, S. Ohshima, Y. Kuriki, K. Yase, and F. Ikazaki, Chem. Phys. Lett. **223**, 65 (1994).
[21] H. Hiura, T. W. Ebbesen, K. Tanigaki, and H. Takahashi, Chem. Phys. Lett. **202**, 509 (1993).
[22] P. V. Huong, R. Cavagnat, P. M. Ajayan, and O. Stephan, Phys. Rev. B **51**, 10048 (1995).
[23] J. M. Holden, P. Zhou, X.-X. Bi, P. C. Eklund, S. Bandow, R. A. Jishi, K. D. Chowdhury, G. Dresselhaus, and M. S. Dresselhaus, Chem. Phys. Lett. **220**, 186 (1994).
[24] P. M. Ajayan, T. W. Ebbesen, T. Ichihashi, S. Iijima, K. Tanigaki, and H. Hiura, Nature **362**, 522 (1993).
[25] G. Wagoner, Phys. Rev. **118**, 647 (1960).
[26] R. J. Elliott, Phys. Rev. **96**, 266 (1954).
[27] J. W. McClure, Phys. Rev. **108**, 612 (1957).
[28] Y. Yafet, Phys. Rev. **85**, 478 (1952).
[29] M. Kosaka, T. W. Ebbesen, H. Hiura, and K. Tanigki, Chem. Phys. Lett. **225**, 161 (1994); **233**, 47 (1995).
[30] D. Pines and P. Slichter, Phys. Rev. **100**, 1014 (1955).
[31] J. Heremans, C. H. Olk, and D. T. Morelli, Phys. Rev. B **49**, 15122 (1994).
[32] A. P. Ramirez, R. C. Haddon, O. Zhou, R. M. Fleming, J. Zhang, S. M. McClure, and R. E. Smalley, Science **265**, 84 (1994).
[33] N. Ganguli and K. S. Krishnan, Proc. R. Soc. London Ser. A **117**, 168 (1941).
[34] E. Poquet, N. Lumbroso, J. Hoarau, A. Marchand, A. Pacault, and D. E. Soule, J. Phys. Chem. **57**, 866 (1960).
[35] M. P. Sharma, L. G. Johnson, and J. W. McClure, Phys. Rev. B **9**, 2467 (1974).
[36] R. R. Gupta, in *Landolt-Börnstein New Series II/16 Diamagnetic Susceptibility*, edited by K.-H. Hellwege and A. M. Hellwege (Springer, Berlin, 1986), Vol. 16, p. 7.
[37] H. Ajiki and T. Ando, J. Phys. Soc. Jpn. **62**, 2470 (1993); **63**, 4267 (1994).
[38] T. Ida and K. Kimura, Z. Phys. (Suppl.) D **26**, 140 (1993).